HIGH-RESOLUTION RADAR MAPS OF THE LUNAR SURFACE AT 3.8-cm WAVELENGTH

S. H. ZISK, G. H. PETTENGILL,* and G. W. CATUNA
Haystack Observatory, Massachusetts Institute of Technology, Westford, Mass., U.S.A.

(Received 30 June, 1973)

Abstract. The entire earth-facing lunar surface has been mapped at a resolution of 2 km using the 3.8-cm radar of Haystack Observatory. The observations yield the distribution of relative radar backscattering efficiency with an accuracy of about 10% for both the polarized (primarily quasi-specular or coherent) and depolarized (diffuse or incoherent) scattered components. The results show a variety of discrete radar features, many of which are correlated with craters or other features of optical photographs. Particular interest, however, attaches to those features with substantially different radio and optical contrasts. An anomaly near 63° is noted in the mean angular scattering law obtained from a summary of the radar data.

1. Introduction

Observations of the Moon by radar over the past two decades have produced much information on the average backscattering properties of the lunar surface over a wide range of wavelengths. The observed distribution of echo power with delay and/or doppler frequency has been interpreted as caused by reflections from a relatively smooth, undulating surface, with the shape of the distribution determined by the average slope of this surface**. In addition to this coherent, quasi-specular component, an incoherent, largely unpolarized diffuse component is seen in the echoes originating some distance from the center of the disk and has been interpreted as originating in wavelength-sized structure, primarily associated with rocks on or near the surface. This interpretation has been strengthened by the discovery of anomalously enhanced, incoherent radar echoes from the region of the crater Tycho (Pettengill and Thompson, 1968), a crater known to be bright on optical photographs, to possess an extensive system of surface rays, and to display a strong thermal enhancement under eclipse conditions.

The first article in this series (I) discussed the general method of high-resolution measurements of the radar backscatter from the lunar surface (Pettengill *et al.*, 1973). Article II (Thompson, 1973) contains the results of such a set of measurements at a wavelength of 70 cm. In this article (III), we present a set of measurements at 3.8-cm wavelength. At this wavelength we expect to be sensitive to roughness at a scale of from 1 to 50 cm, as compared to a scale of 20 to 1000 cm at 70-cm wavelength. A comparison of the data at the two wavelengths with each other and with optical photographs and other data yields clues to the age and history of many features of the

* Now at Department of Earth and Planetary Sciences, M.I.T.
** See Evans and Hagfors (1971) for an excellent review and bibliography.

The Moon **10** (1974) 17–50.

lunar surface. Some rudimentary conclusions from the 3.8 cm data alone are given at the end of this paper. The last article (IV) in this series presents a more elaborate analysis of a variety of lunar features, incorporating both sets of radar data as well as other sources of information.

The high-resolution radar maps have revealed a number of unusually strong radar backscattering regions, some of which are correlated with bright optical features and some with regions having atypically large thermal conductivity. It appears that the radar data may permit differentiation among surface features that are not so clearly distinguished by other means.

This paper describes the latest 3.8-cm measurements of the Moon, and presents a summary of the results as a series of maps of the 'polarized' and 'depolarized' radar echoes*. Section 2 of this paper contains a description of the experiment insofar as it differs from the general description given in Article I, and explains the calibrations and sources of inaccuracy in determining the selenographic coordinates and backscattered power. Section 3 describes the results in general terms, and also contains a brief analysis of several regions of the surface in some detail.

2. Experiment

A. GENERAL DESCRIPTION

The purpose of the radar measurements presented here was to obtain highly resolved maps of the surface scattering characteristics at a wavelength of 3.8 cm from the entire earthside hemisphere of the Moon. While the radar surface resolution of about 2 km is only slightly worse than the best obtainable at optical wavelengths with earth-based telescopes, the scattering in the two cases is presumable associated with very different scales of surface structure. Thus the combination is a powerful aid in understanding surface geometry. The radar resolution was obtained with coherent-pulse analysis ('delay-doppler mapping') as described in Article I, using the Haystack radar and post-processing system. The detailed parameters used in the observations are listed in Table I.

Each lunar observation (run) at Haystack, using the two-way, half-power angular beam diam of 3.1 arc min, could cover a projected area on the lunar surface with an extent of about 400 km. For simplicity, a standard mapping unit on the lunar surface with a size of approx 380 km was adopted. Through the selection of one of five different pulse lengths (see Table I) the delay resolution projected on the lunar surface was kept at approx 2 km for all observations. A series of 190 successive time samples, at intervals of the pulse length, covered the standard mapping unit in each case.

A similar adjustment of the frequency resolution was made through the choice of interpulse interval (reciprocal of the pulse repetition frequency), so that the corresponding surface resolution would also be approx 2 km in the direction of maximum

* The term 'polarized' as used in this paper has the usual meaning: that sense of echo polarization which corresponds to specular reflection from a smooth plane interface at normal incidence. The term 'depolarized' corresponds to the orthogonal sense.

TABLE I

Radar parameters for lunar observations

Wavelength (frequency)	3.83 cm (7840.0 GHz)
Polarization	
Transmitted	Right-circular
Received	Left (polarized) and right (depolarized) circular, simultaneously
Transmitter	
Power	200 kW (peak)
Pulse length	3, 4, 5, 7, 10, or 13 μs
Interpulse period	25–90 ms (adjusted for that frequency resolution corresponding to 2 km on the surface)
Frequency standard utilization	Hydrogen maser or rubidium standard All transmitter, receiver, and timing functions
Precision	Better than a part in 10^{11}
Receiver	
System temperature	
Polarized	45K (sky); 180K (moon)
Depolarized	75K (sky); 210K (Moon)
Operating Frequency	7840.0 GHz + Doppler offset to center of mapped area
Setting accuracy	$\pm$0.01 Hz
Resetting interval	10 ms
Antenna	
Gain	66 dB
Effective area ($=\eta\pi R^2$)	460 m^2
Beamwidth (one way)	4.4 arc min (full-width at half-power)
(two-way)	3.1 arc min (full-width at half-power)
Pointing	$\pm$20 arc sec
Real-time processing	
Computer	Control Data Corp. Model 3300
Samples per received pulse	190
Calibration samples per interpulse	26 (20 usable)
Sample interval	3–13 μs (to match transmitter pulsewidth)
Post-processing	
Number of pulses coherently analyzed	256
Duration of Coherent Integration Period (CIP)	6 to 26 s ($=256\times$ interpulse period)
Number of CIP's per map	85 ± 5
Fluctuation of backscatter values	11 % rms
Normalization parameters	
Two-way beam shape	exp ($-0.278\ \phi^2$) (ϕ in arc min)
Background noise level per received pulse	As measured at 1.0 ms prior to first lunar echo
Assumed scattering law	Depolarized: $S(\theta)=\cos(\theta)$ Polarized: Analytic approximation to Evans 3.6-cm results (Evans and Hagfors, 1971)
Area of resolution cell	
Range-Doppler coordinates	Rectangular, = pulsewidth $\times$ frequency resolution
Lunar surface coordinates	Same, projected onto spherical lunar surface

Table I (Continued)

Additional corrections	Transmitted power
	Earth–Moon distance
	Background level
	Receiver gain
Mapping parameters	
Observed coordinates	Delay-doppler
Projected surface	1738.0-km sphere
Final map projections	Mercator, Lambert Conformal
Error in absolute locations	± 4 km (rms)
	± 20 km (maximum)

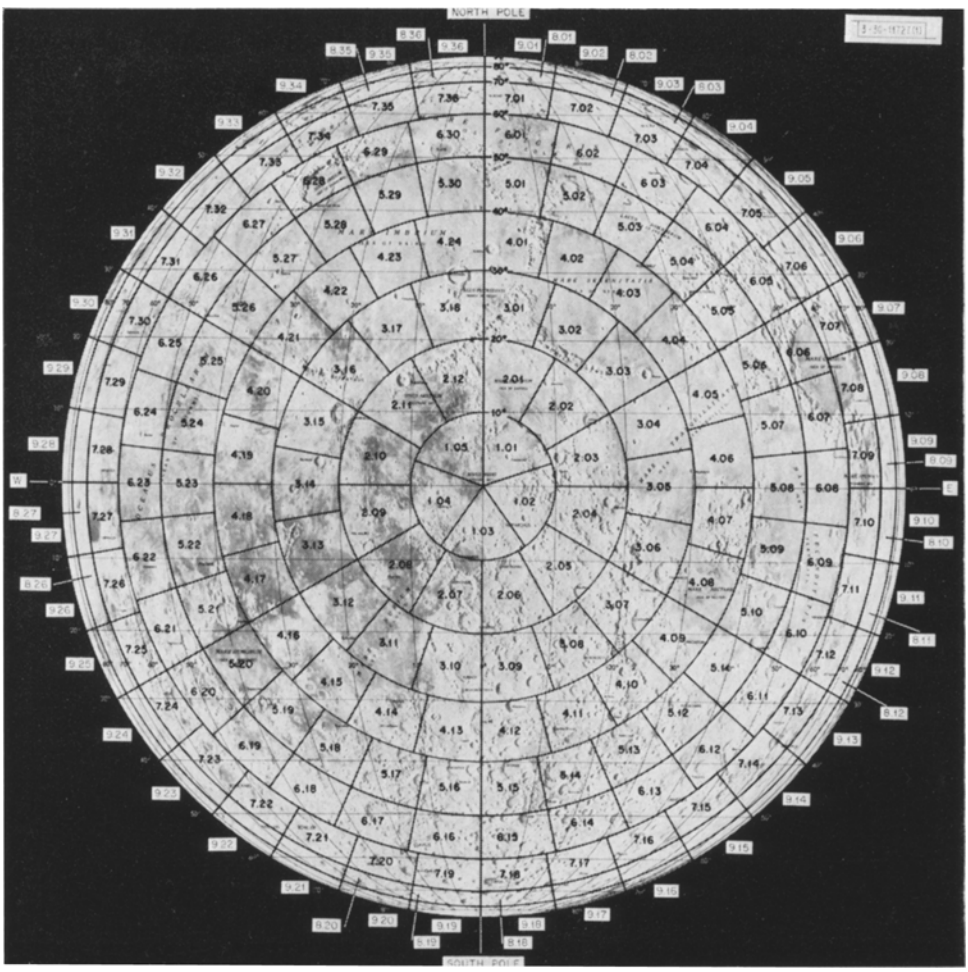

Fig. 1. Location of ZAC-area observing units on the lunar surface.

doppler shift. Note that observations were scheduled for a given area only when the projection of the delay-doppler isopleths in that area were nearly orthogonal, i.e., the observed areas were all relatively close to the axis of apparent rotation. Therefore, since a 256-point Fast Fourier Transform (FFT) was used in analyzing all runs, no frequency folding (at intervals of 512 km) could occur within the illuminated area (less than 400 km in extent).

In order to insure efficient coverage of the near side of the Moon, a system of subareas was set up whose boundaries were roughly parallel to the isopleths of the delay-doppler coordinates. The earthside hemisphere was divided into nine concentric ZAC (Zenith-Azimuth Coordinate) zones, each 10° deep, and centered on the selenographic origin. A tenth zone accommodated areas which are occasionally in view as a result of libration. Each zone was further subdivided in azimuth to produce ZAC-areas containing roughly equal areas of the Moon's surface. A map of the ZAC-area system appears in Figure 1.

B. SELENOGRAPHIC MAP COORDINATES

During each observation, the radar receiver was adjusted continuously to follow the predicted values of delay and doppler shift for the center of the mapping unit under observation. This center point then became the reference for the remainder of the map. Any time-varying error in the prediction ephemerides would cause blurring of the map, whereas an error that remained constant during the 10-min observation would only displace the map in the delay or doppler directions.

The range and range-rate of the center of mass of the Moon were predicted as outlined in Article I, from the Nautical Almanac (i.e., Brown's theory) and from Brown's theory as corrected by Eckert. No attempt was made in the reduction of the maps themselves to compensate for the lunar topography; in all cases, a radius of 1738.0 km was assumed for the location of the backscattering element. The total discrepancy in range between predictions and observations was less than 6 km, and all but 0.5 to 1.0 km later proved to be the result of a combination of small errors in the working ephemeris (as compared to currently best-known values), and topography near the subradar point.

The observed discrepancies in the doppler frequency also appear to be related partly to the ignored topography, and partly to minor errors in the working ephemeris. The largest contribution to the error, however, appeared to be associated with the topocentric-libration ephemeris. Here, a combination of a simplified method of libration calculation, together with the necessarily unrefined physical libration model available in 1968, resulted in errors of as much as 1 cm s^{-1} in the predicted range rate for a given surface point. In the mosaic which results from combining many mapping units, this error is uncorrected and has the effect of distorting the relative locations of a few parts of the map by as much as 20 km (0.7° selenographic). We have recently prepared a reprocessing method that can eliminate most of the distortion, by incorporating into the maps a newer version of the lunar libration ephemeris. Figure 2 is a radar map of LAC 39, the Aristarchus quadrangle, showing the excellent coordinate

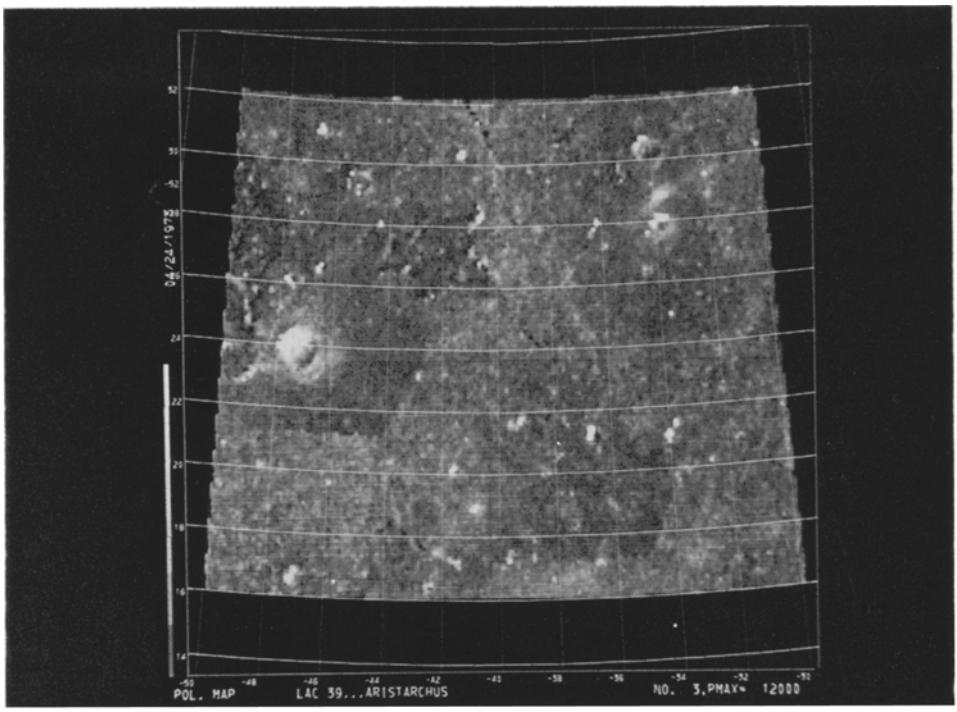

(a)

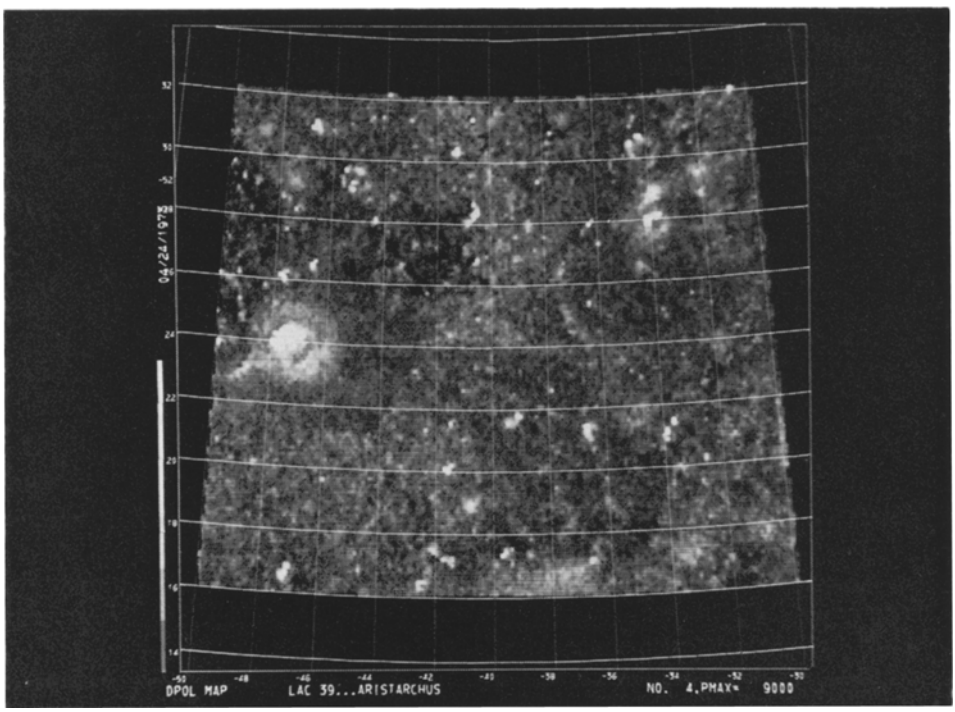

(b)

Fig. 2. LAC 39, Aristarchus Quadrangle: 3.8-cm radar mosaic map, illustrating the potential improvement in radar-derived coordinate systems, (a) Polarized map, (b) Depolarized map.

match that is now attainable. Figure 2 may be compared with the appropriate parts of Figure 5, to see the full extent of the improvement.

C. ACCURACY: CALIBRATION AND NORMALIZATION

The maps were calibrated essentially as outlined in Article I. In an attempt to improve the absolute values of observed radar cross section, the gain of the receiver was continuously measured by switching in a noise-calibration signal during half of the background noise sampling interval described in Article I (Section D). This procedure minimized inaccuracies caused by the radar system, but could not remove the effects of atmospheric absorption. (Calibration to standard lunar areas would have been preferable, but would have double the required observing and analysis time and complexity of the project.)

The final backscatter values appear to have an internal consistency of better than $\pm 20\%$ over most of the observed lunar surface, but observations near the lunar equator occasionally appear to be miscalibrated and may be low by factors of as much as 3 or 4. The results are always lower than expected, which suggests anomalous atmospheric attenuation as a possible cause, since most of the equatorial areas were observed at low elevation angles to obtain a proper delay-doppler geometry.

3. Results

Figures 3 to 8 are photographic representations of the results of the 3.8 measurements, covering the entire earthside hemisphere and a part of the libration zone*. Figure 3 shows the entire earthside hemisphere in a series of 5 mosaics each for the polarized (Figure 3a) and depolarized (Figure 3b) radar return. The equatorial band in the center of each figure covers the region between 16° N and 16° S latitude on a Mercator projection, and is therefore comparable with the well-known Lunar Aeronautical Chart series from LAC 55 through 63 and LAC 73 through 81 (Air Force Chart and Information Center, St. Louis, various dates). The other four bands in each figure are also given in the same Lambert Conformal projections as the corresponding LAC-charts, with the exception of the polar regions (higher than 80° latitude). Here, the LAC-charts are presented in Polar Stereographic projection, but for simplicity in the radar maps these small areas are included with the remainder of the polar region in the corresponding Lambert projection.

In Figures 4–8 the individual bands of Figure 3 have been enlarged to provide more detail. The polar regions appear in their entirety in Figures 4 and 8, while the remaining three bands have been divided into 5 equal sections and are shown in Figures 5.1–5.5 (North Temperate Band), 6.1–6.5 (Equatorial Band), and 7.1–7.5 (South Temperate Band). In each case, the polarized (subscript *a*) and depolarized (subscript *b*), maps are shown on the same page for ease of comparison.

In general, the depolarized maps show only the diffuse reflection from the surface,

* Three ZAC areas in the 9th ring are missing as a result of observational problems that were not discovered until too late for re-observation: 9.06, 9.13, and 9.17.

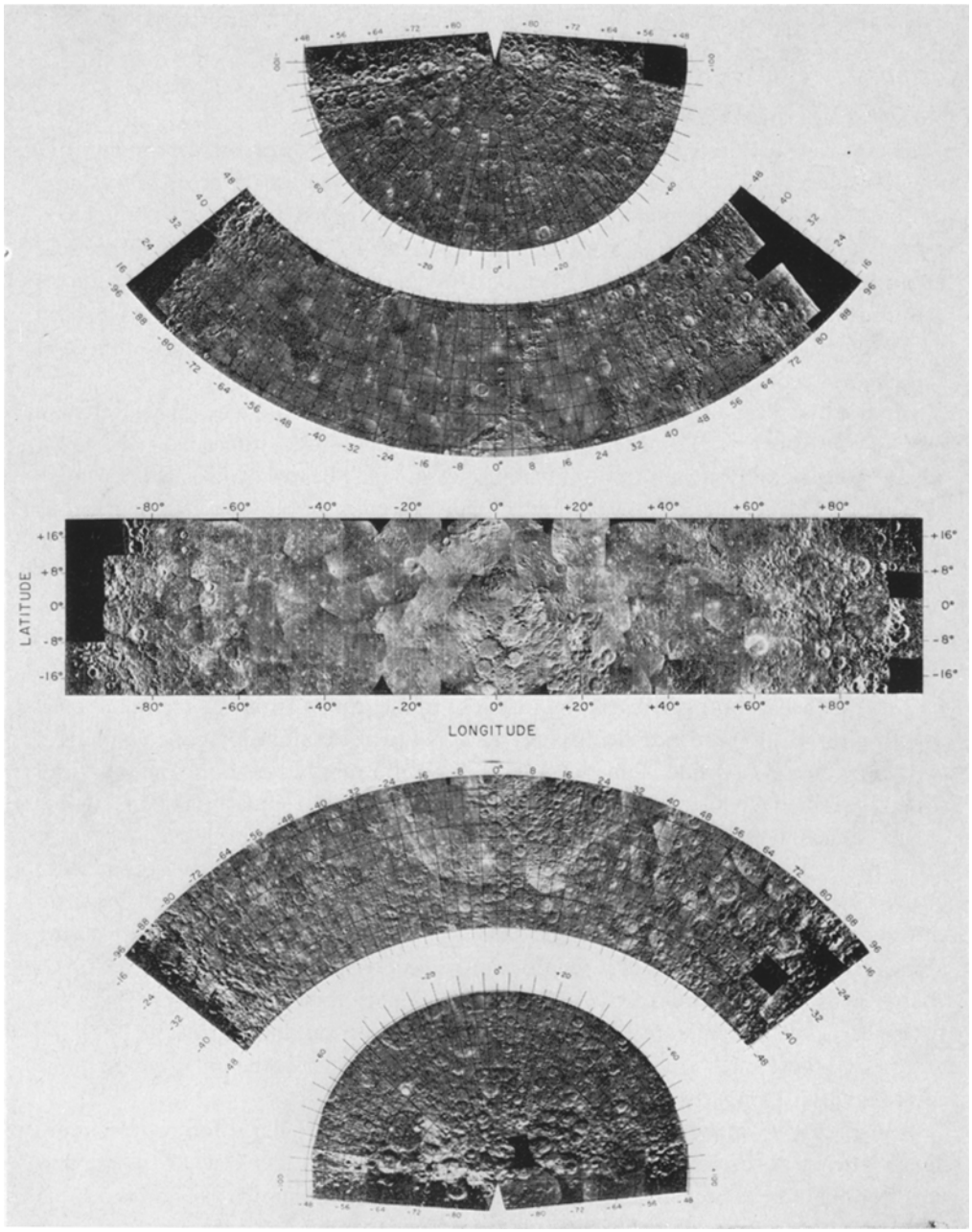

Fig. 3a. Overall map of the polarized component of the radar backscatter from the earthside hemisphere.

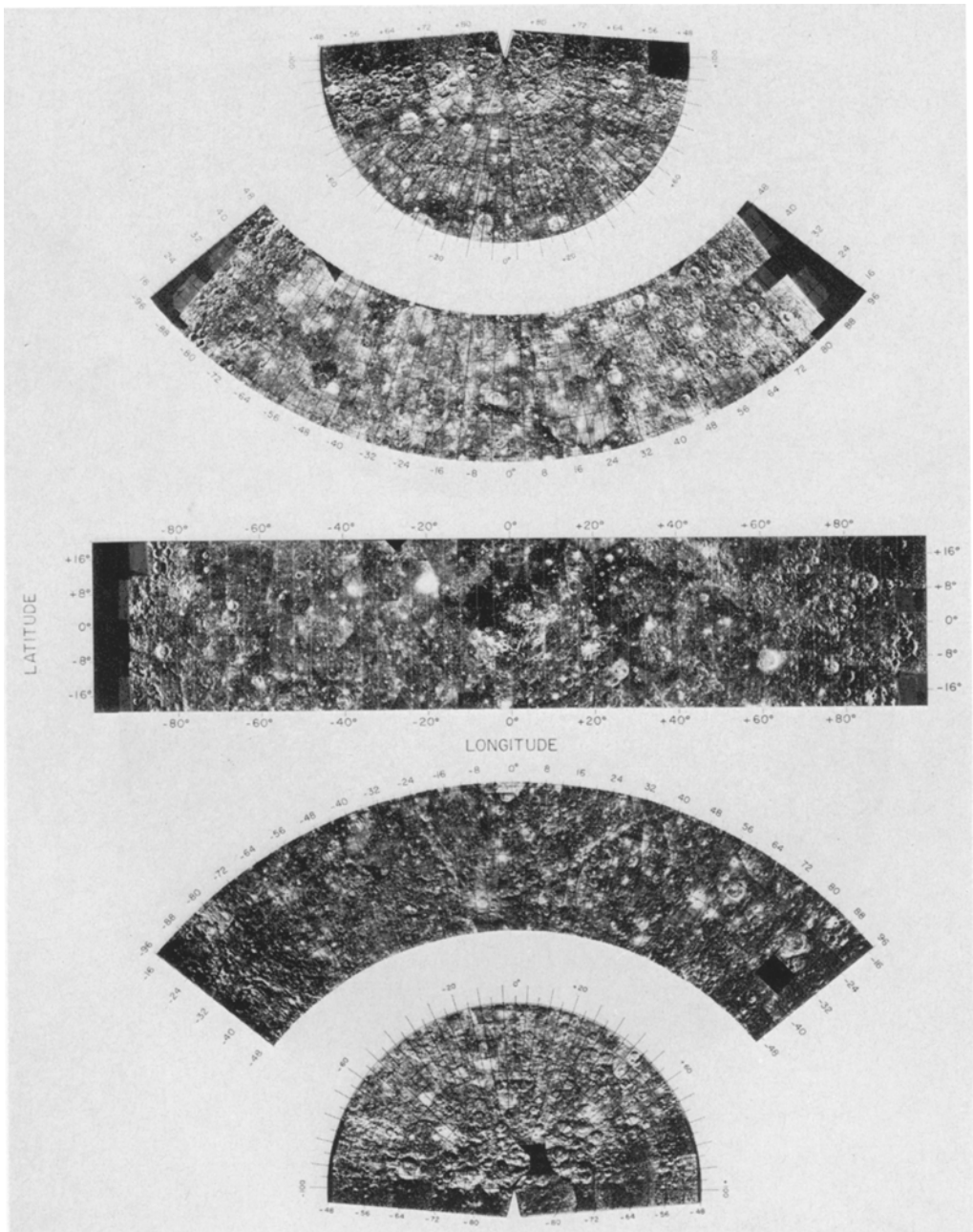

Fig. 3b. Overall map of the depolarized component of the radar backscatter from the earthside hemisphere.

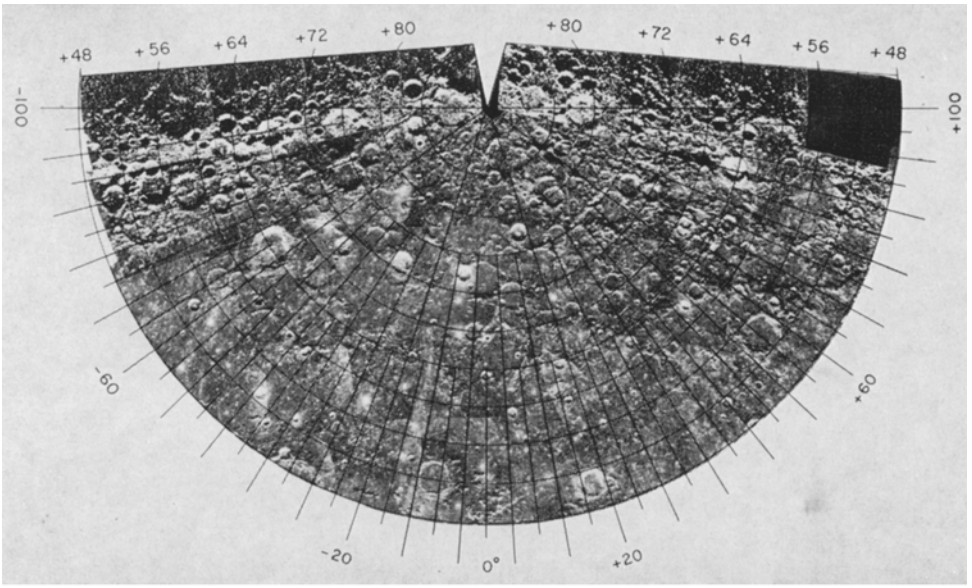

(a)

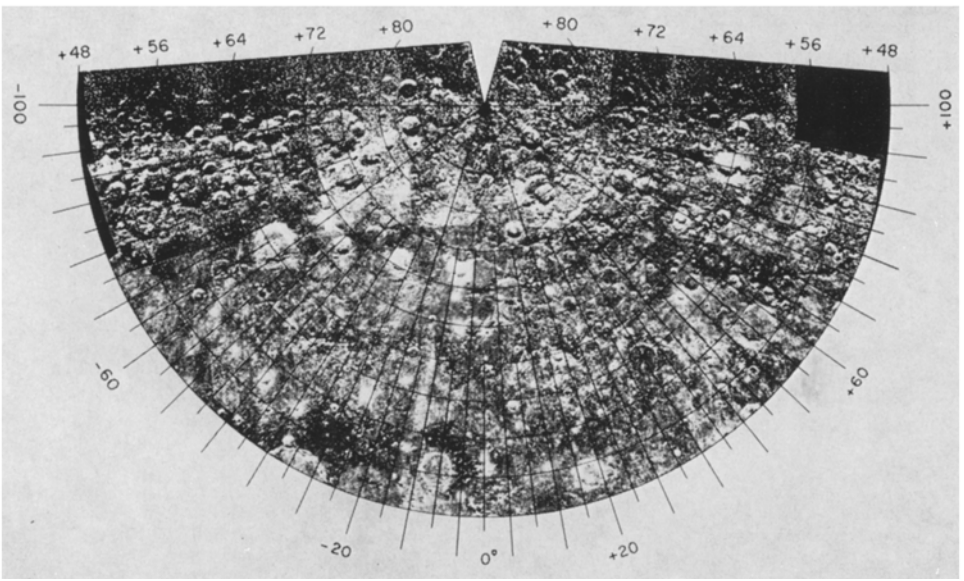

(b)

Fig. 4. North Polar Belt: (a) Polarized, (b) Depolarized.

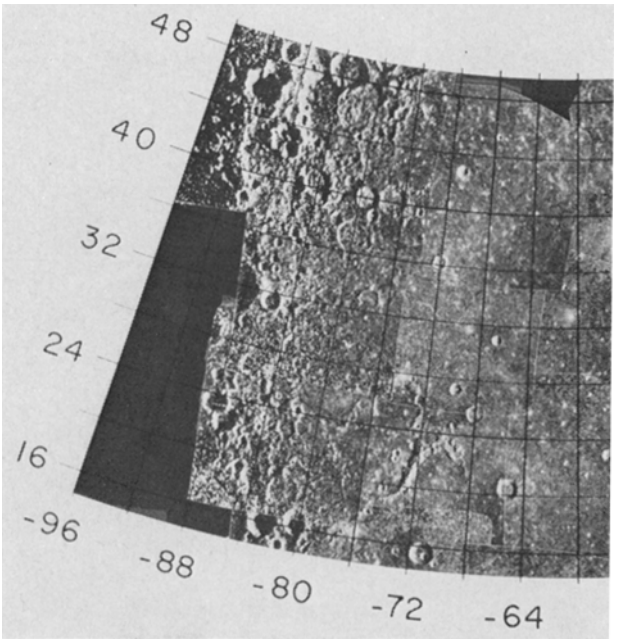

(a)

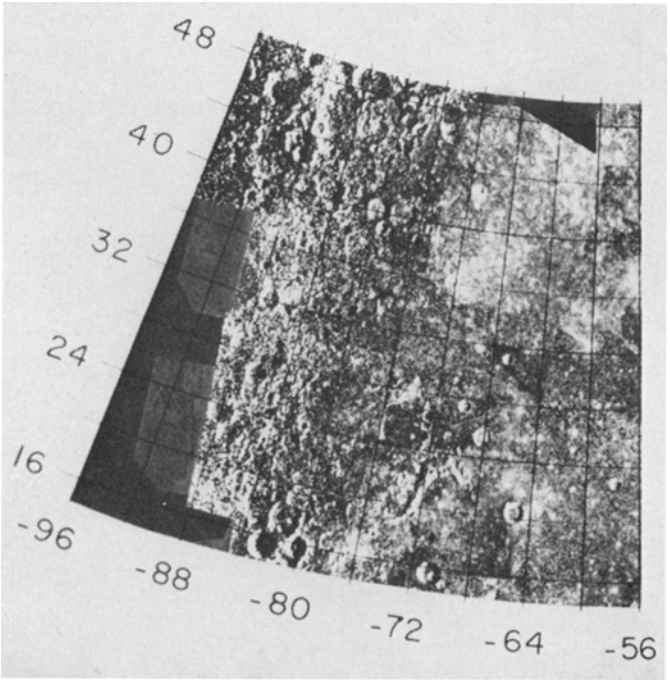

(b)

Fig. 5.1. Western limb, North Temperate Belt: (a) Polarized, (b) Depolarized.

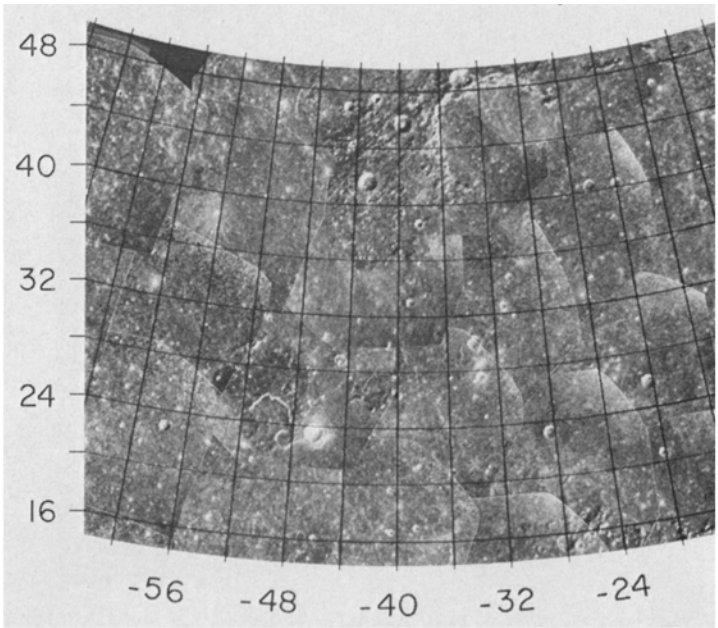

(a)

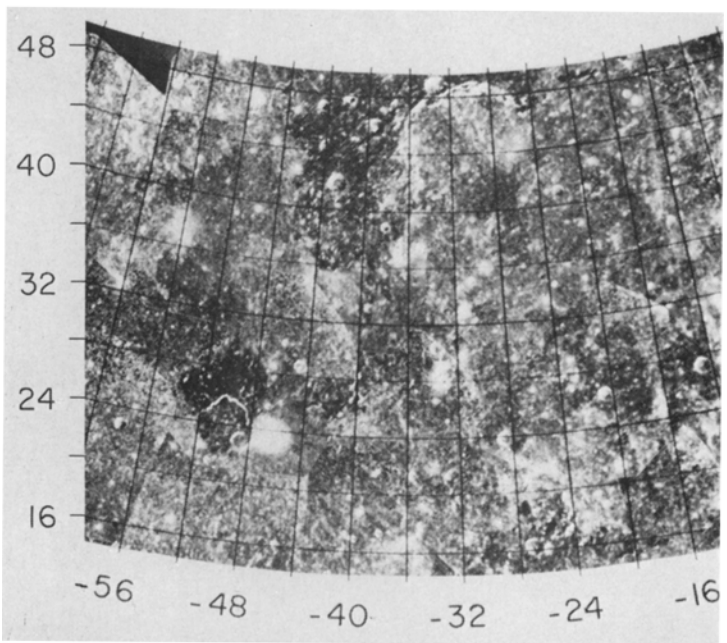

(b)

Fig. 5.2. Middle-western region, North Temperate Belt: (a) Polarized, (b) Depolarized.

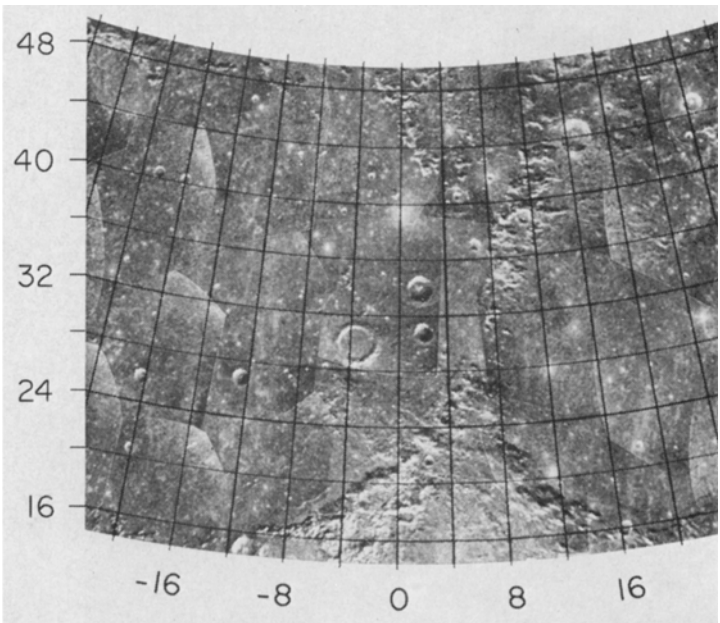

(a)

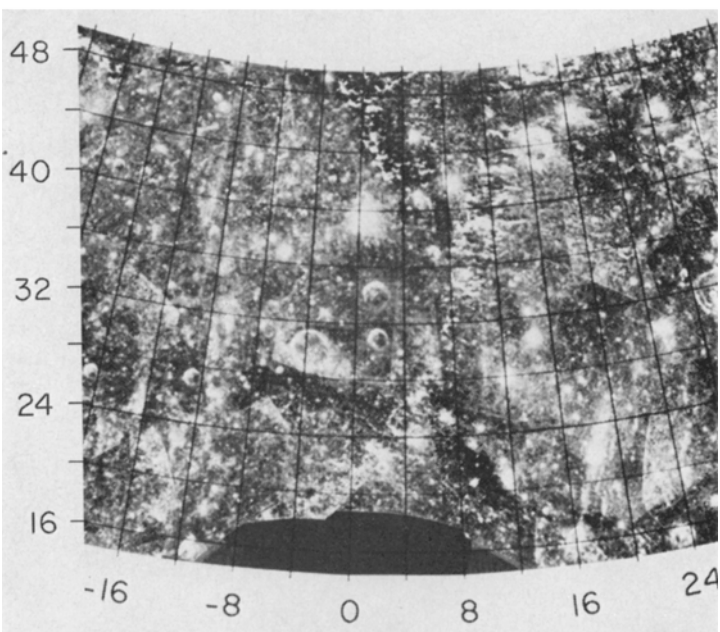

(b)

Fig. 5.3. Central region, North Temperate Belt: (a) Polarized, (b) Depolarized.

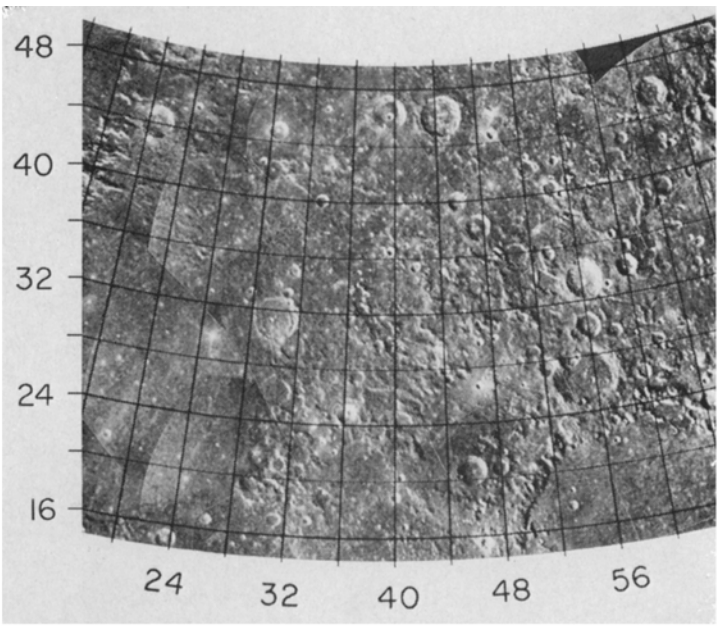

(a)

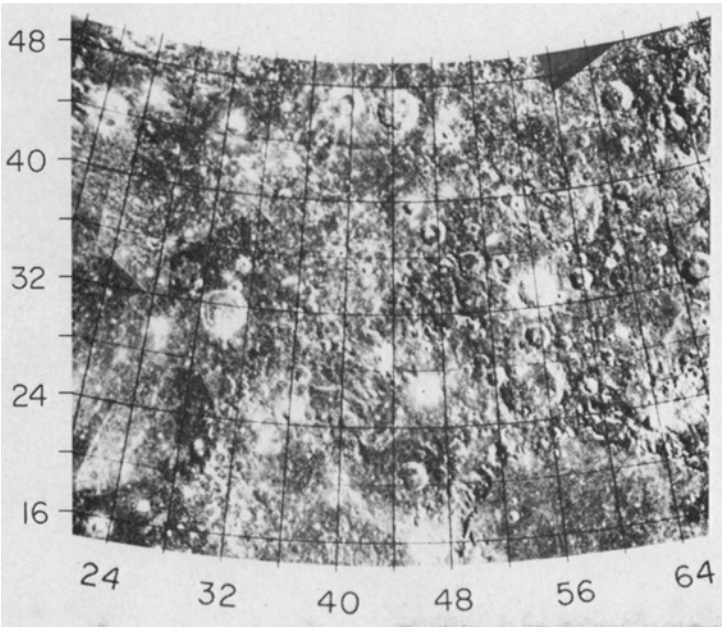

(b)

Fig. 5.4. Middle-eastern region, North Temperate Belt: (a) Polarized, (b) Depolarized.

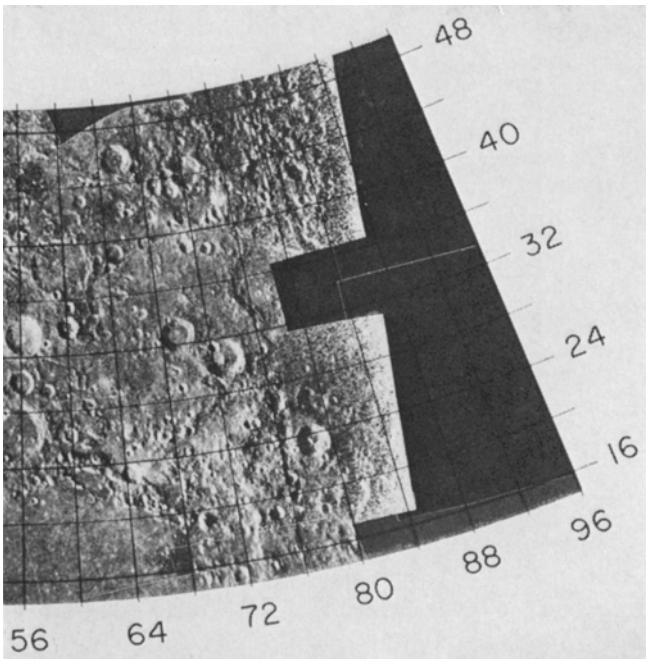

(a)

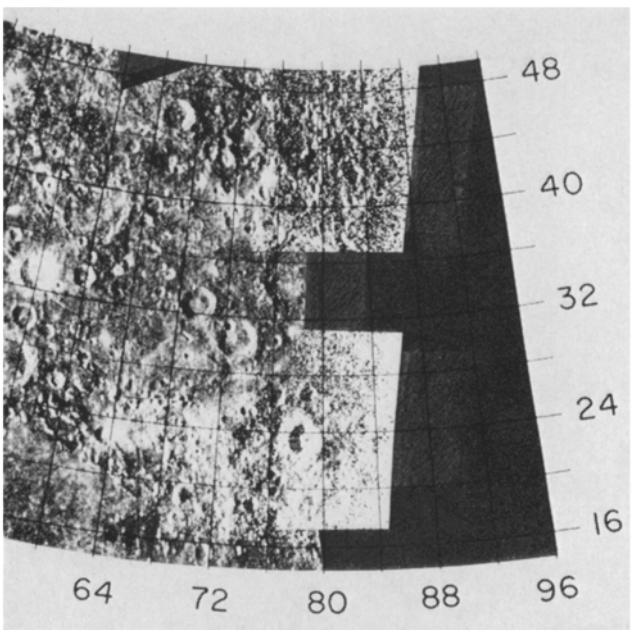

(b)

Fig. 5.5. Eastern limb, Equatorial Belt: (a) Polarized, (b) Depolarized.

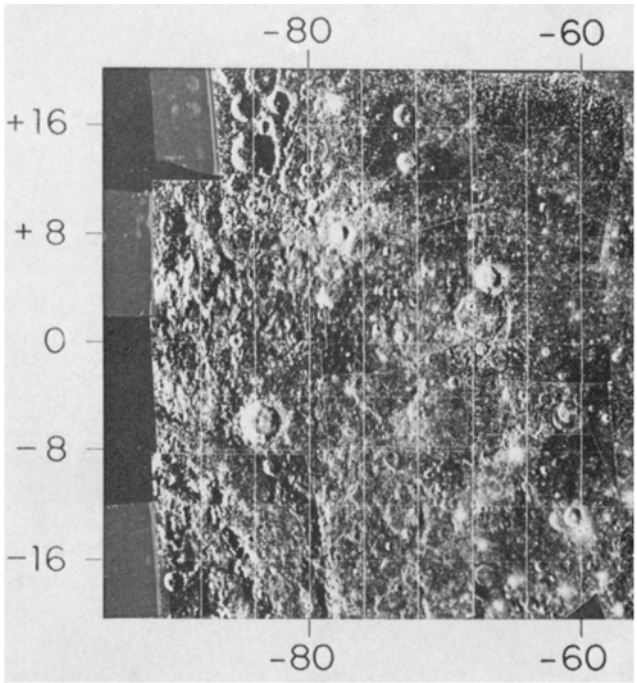

(a)

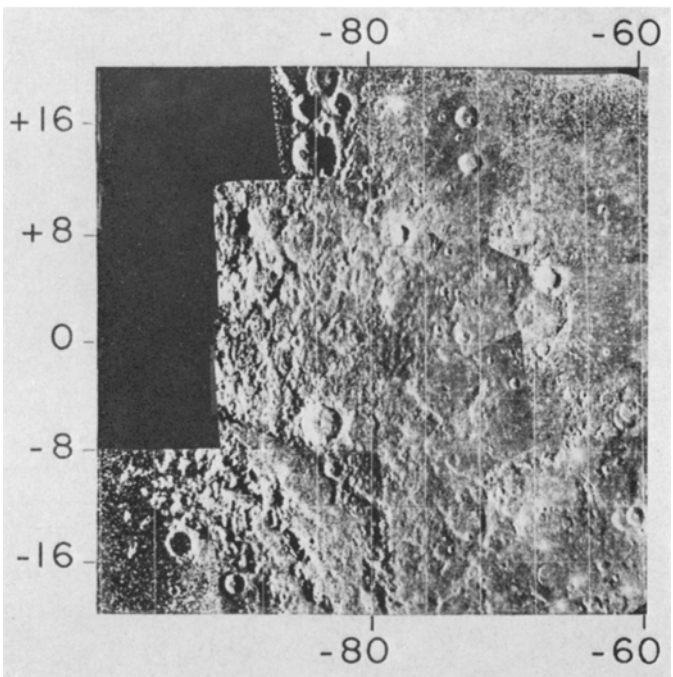

(b)

Fig. 6.1. Western limb, Equatorial Belt: (a) Polarized, (b) Depolarized.

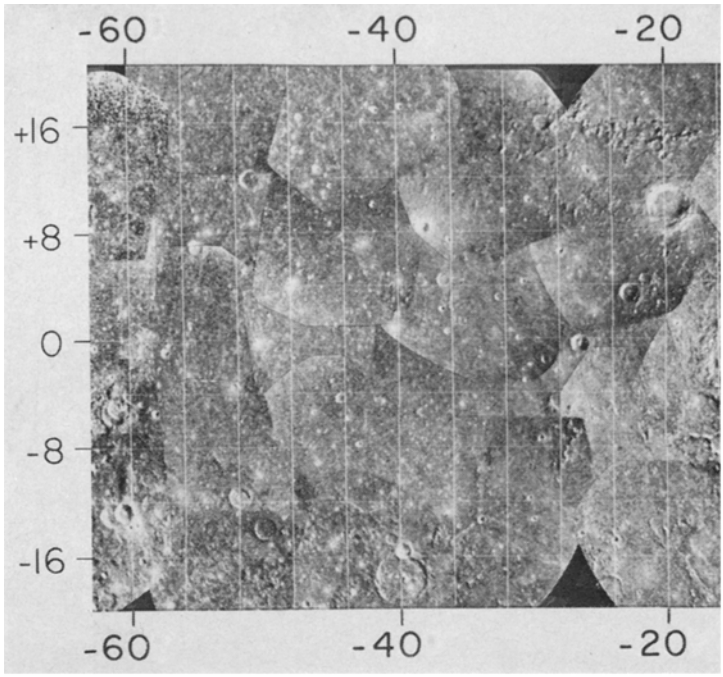

(a)

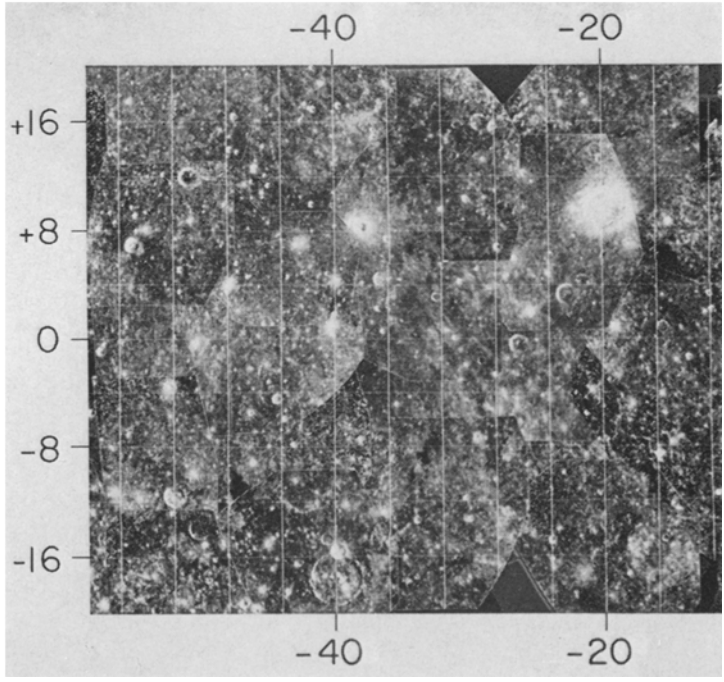

(b)

Fig. 6.2. Middle-western region, Equatorial Belt: (a) Polarized, (b) Depolarized.

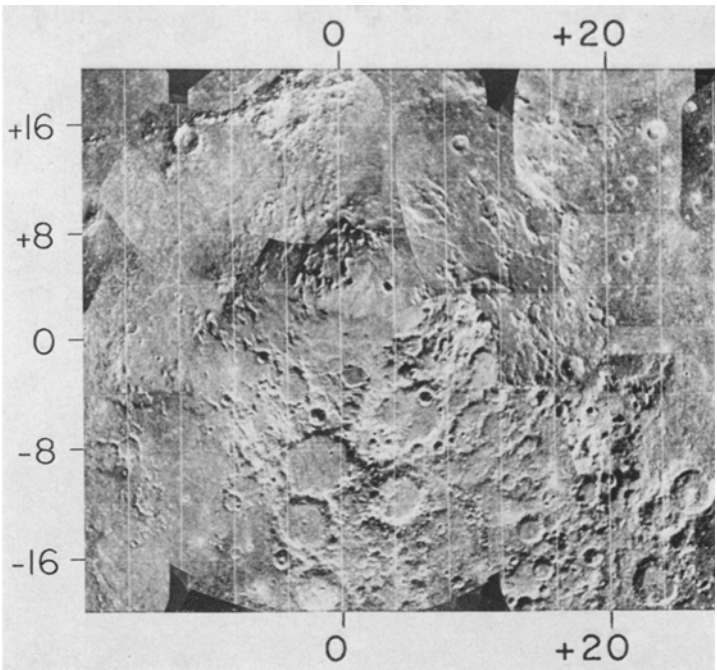

(a)

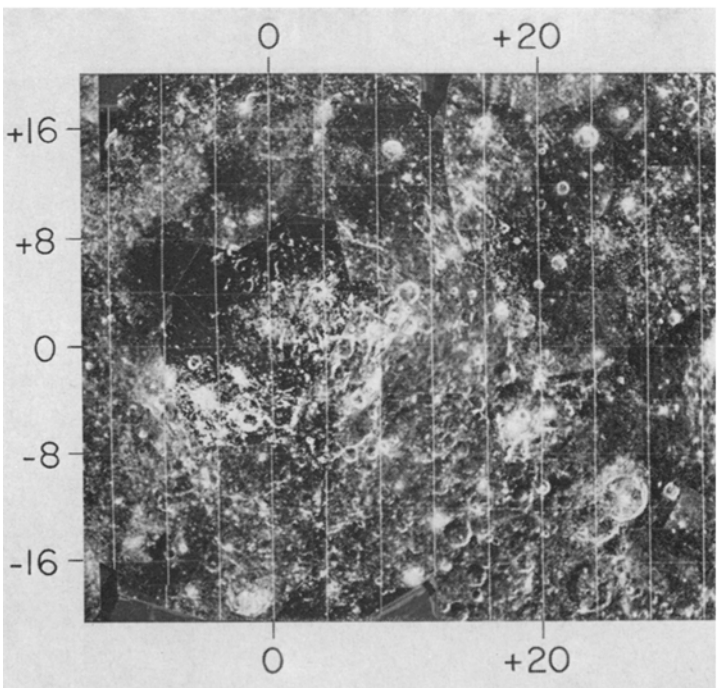

(b)

Fig. 6.3. Central region, Equatorial Belt: (a) Polarized, (b) Depolarized.

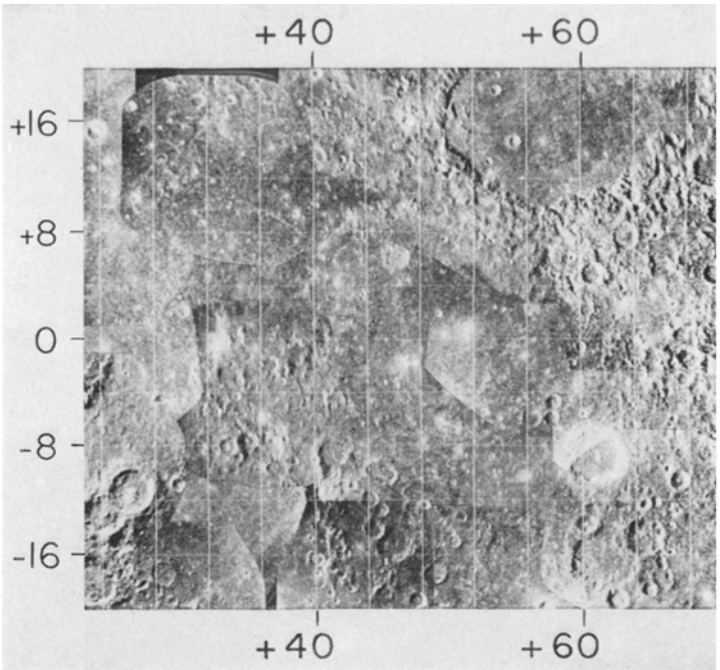

(a)

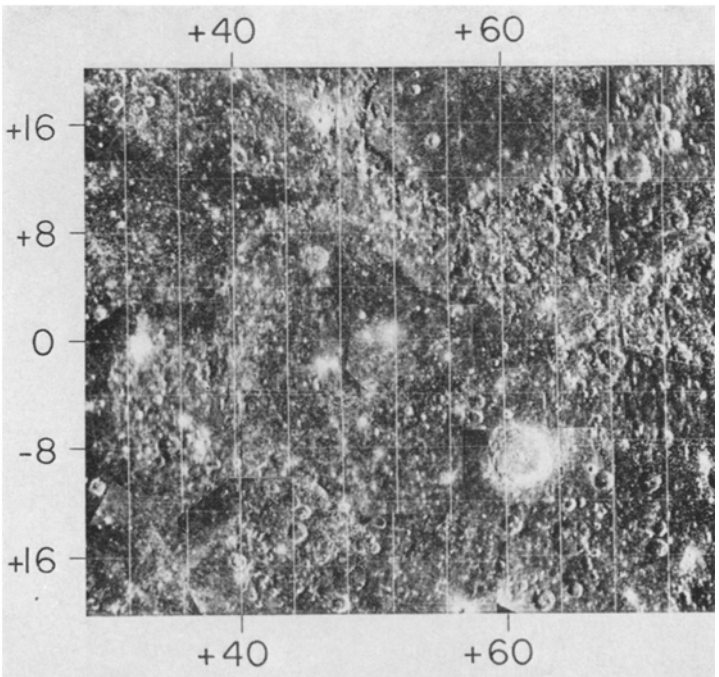

(b)

Fig. 6.4. Middle-eastern region, Equatorial Belt: (a) Polarized, (b) Depolarized.

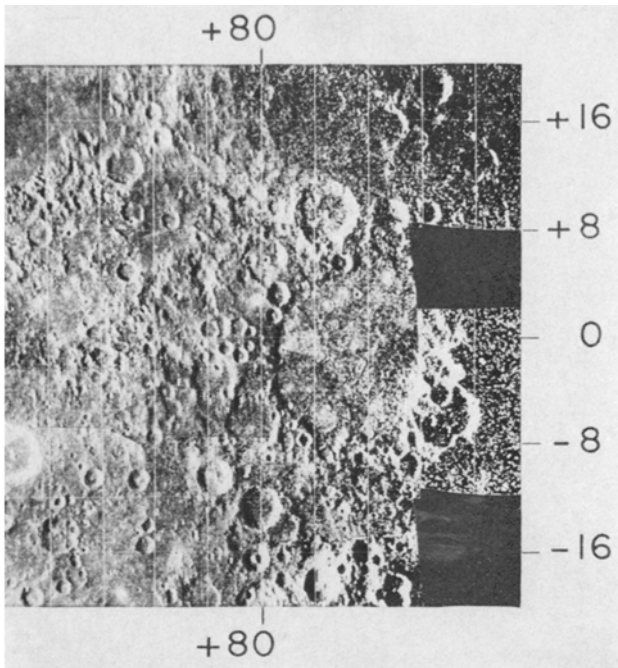

(a)

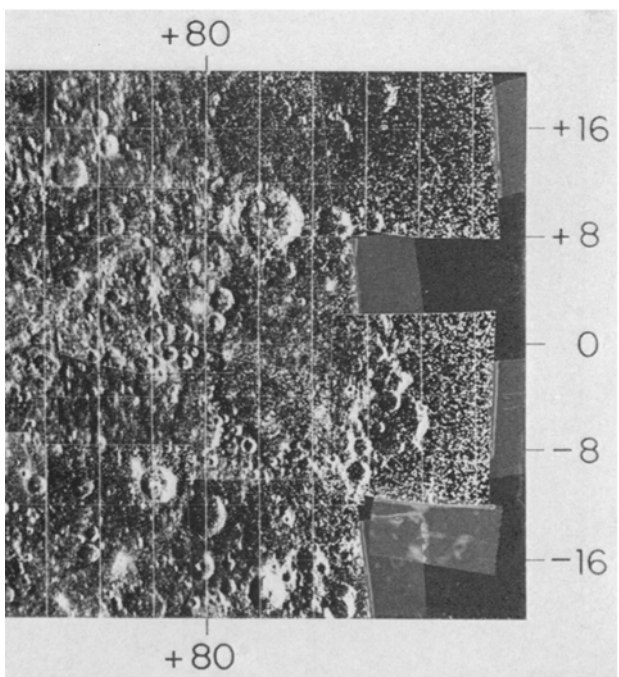

(b)

Fig. 6.5. Eastern limb, Equatorial Belt: (a) Polarized, (b) Depolarized.

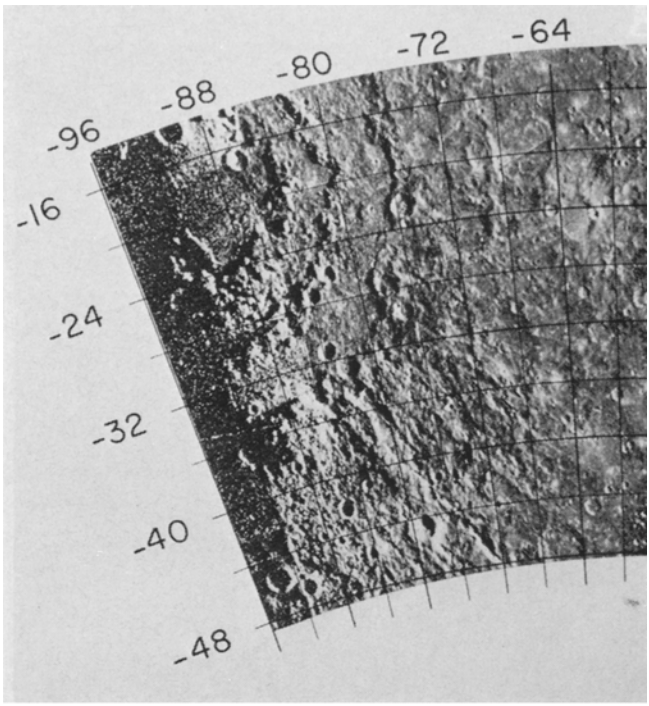

(a)

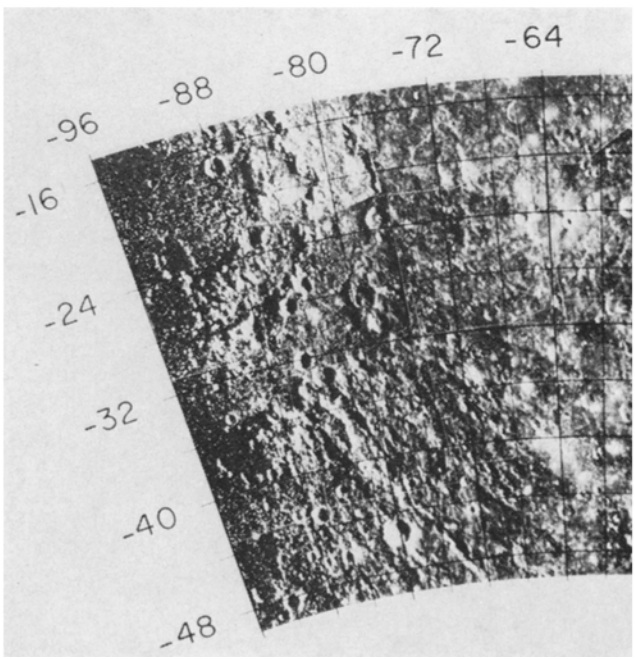

(b)

Fig. 7.1. Western limb, South Temperate Belt: (a) Polarized, (b) Depolarized.

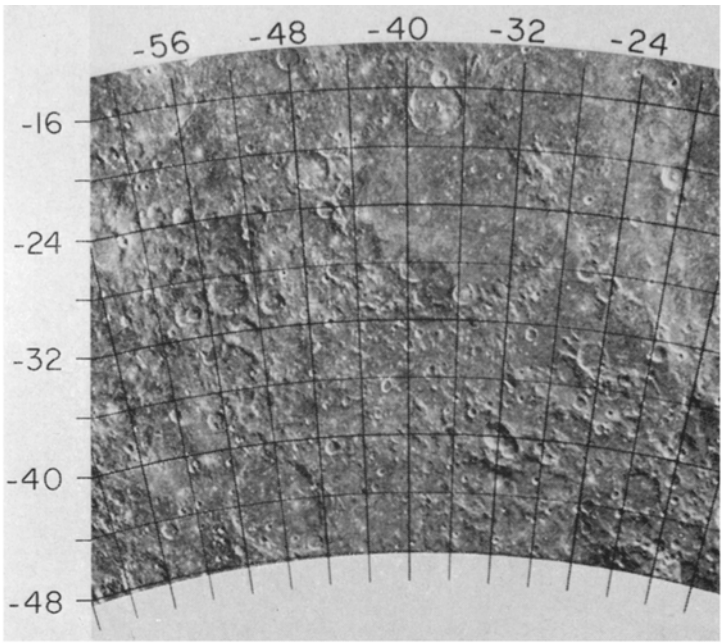

(a)

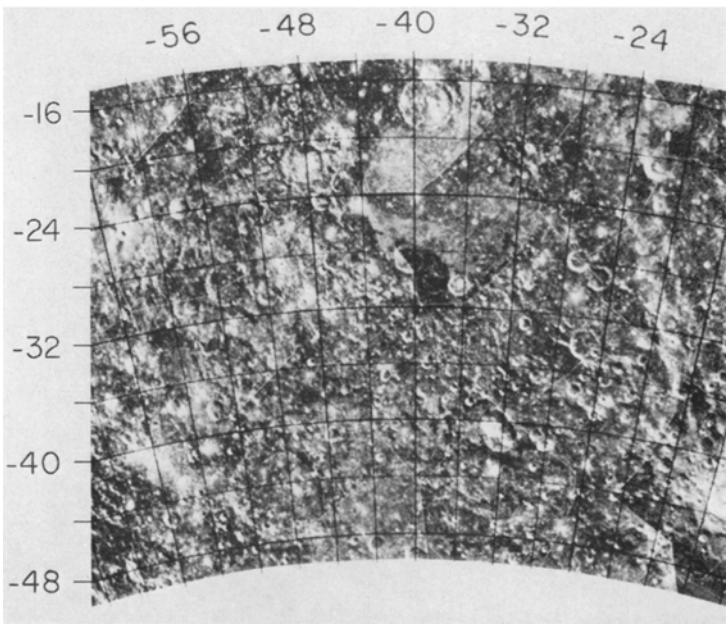

(b)

Fig. 7.2. Middle-western region, South Temperate Belt: (a) Polarized, (b) Depolarized.

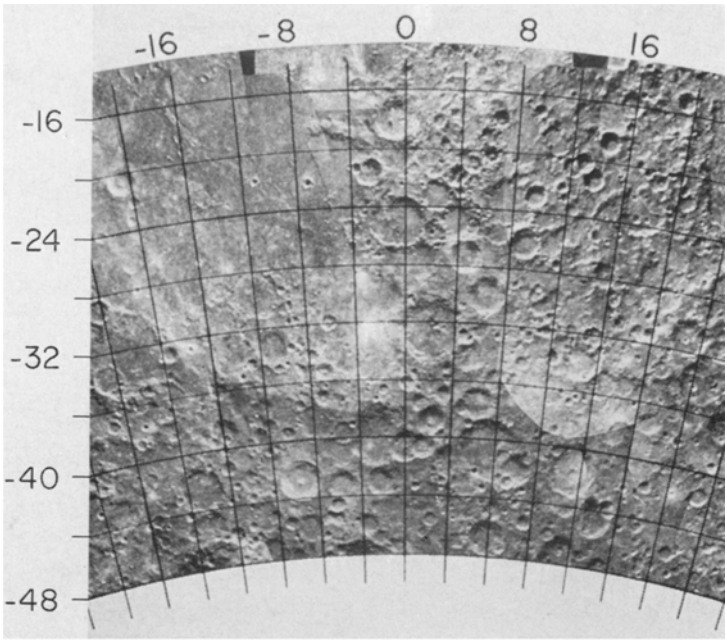

(a)

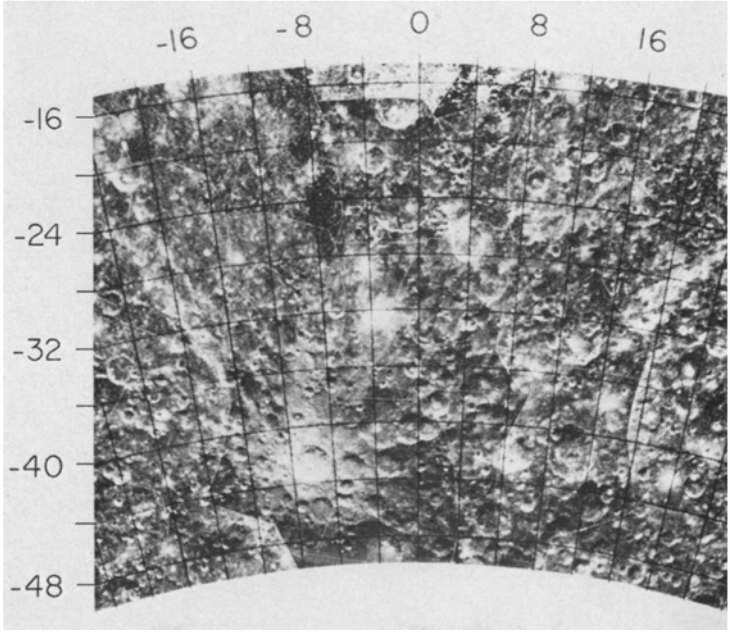

(b)

Fig. 7.3. Central region, South Temperate Belt: (a) Polarized, (b) Depolarized.

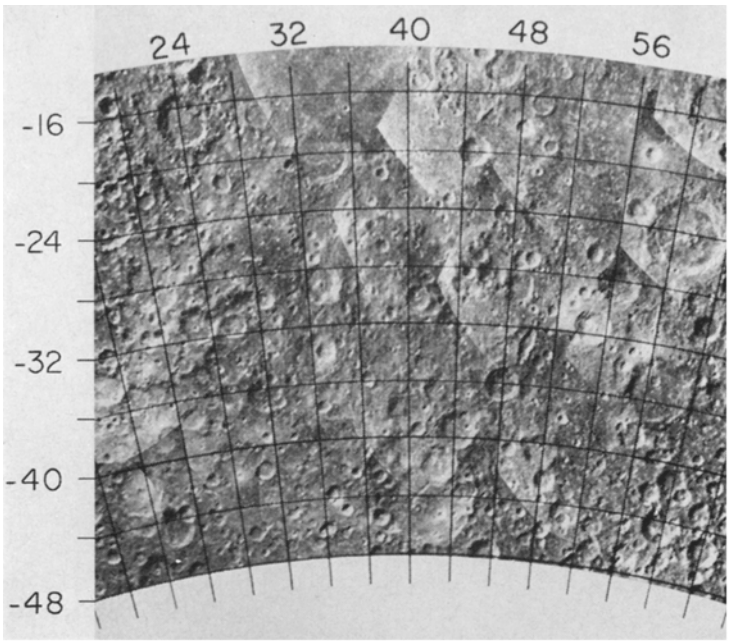

(a)

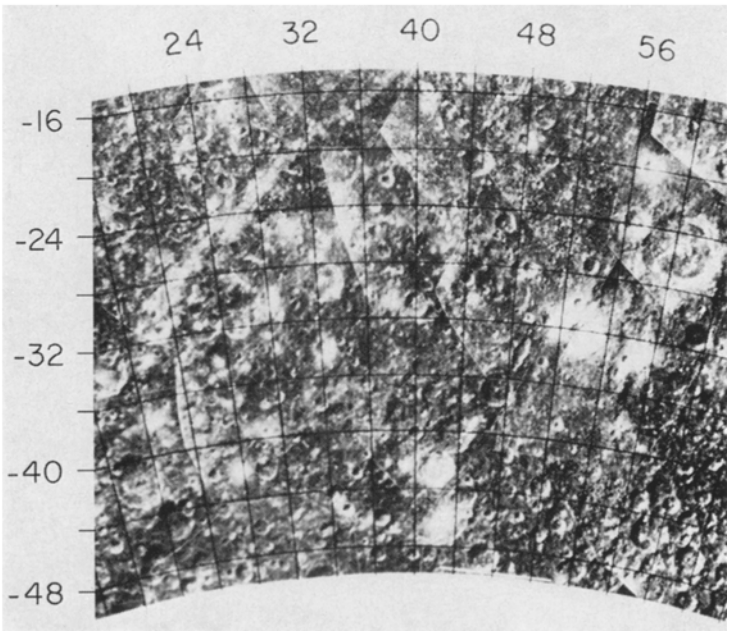

(b)

Fig. 7.4. Middle-eastern region, South Temperate Belt: (a) Polarized (b) Depolarized.

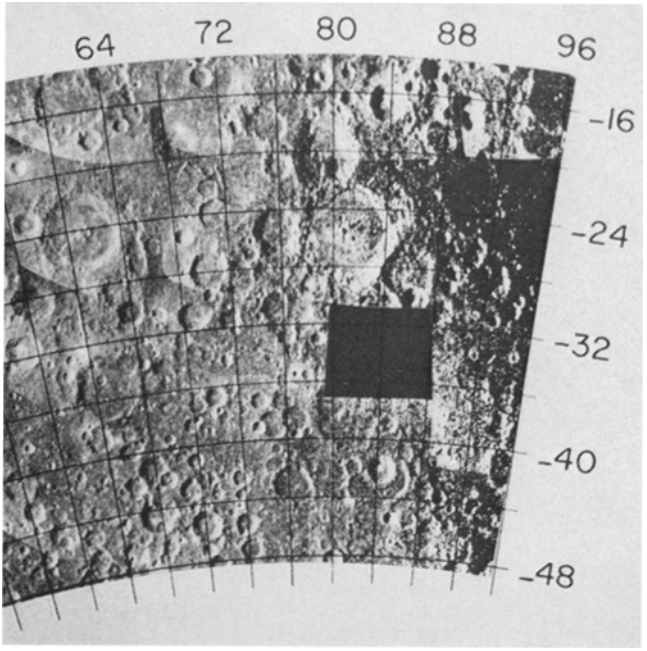

(a)

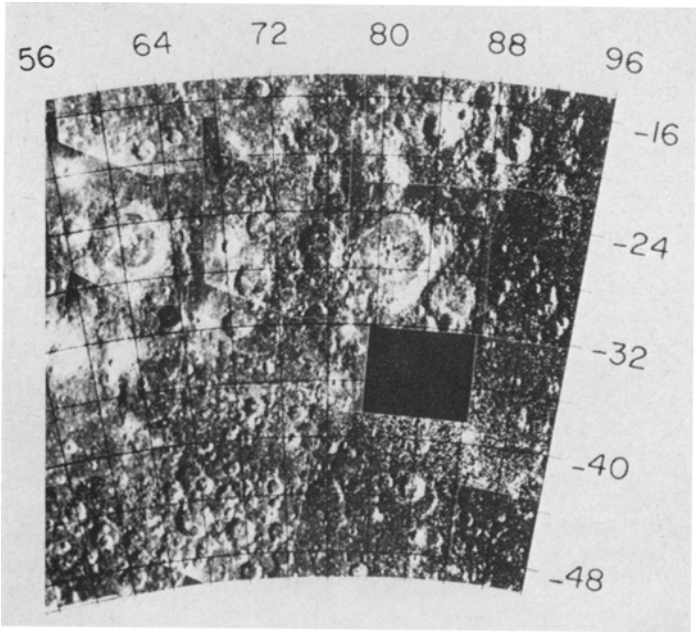

(b)

Fig. 7.5. Eastern limb, South Temperate Belt: (a) Polarized, (b) Depolarized.

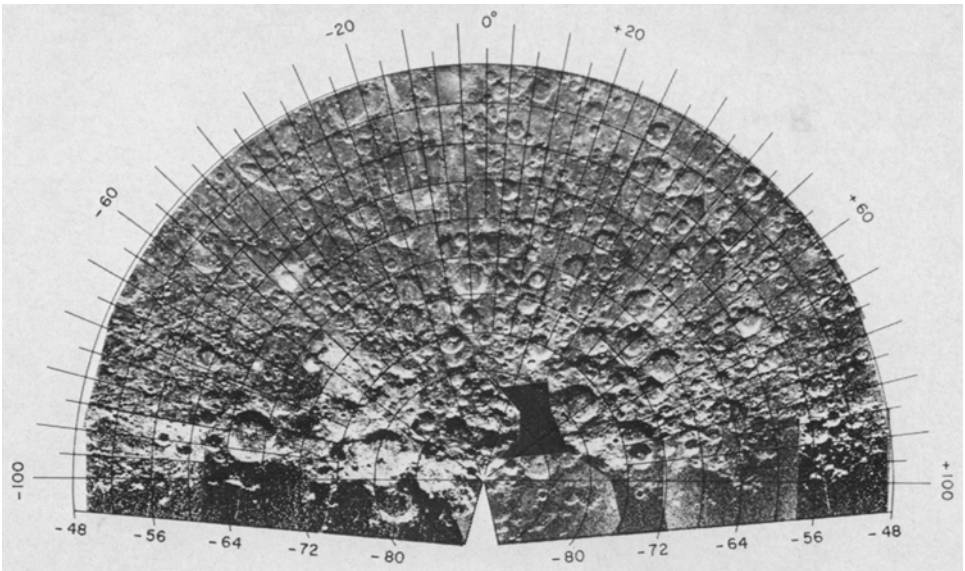

(a)

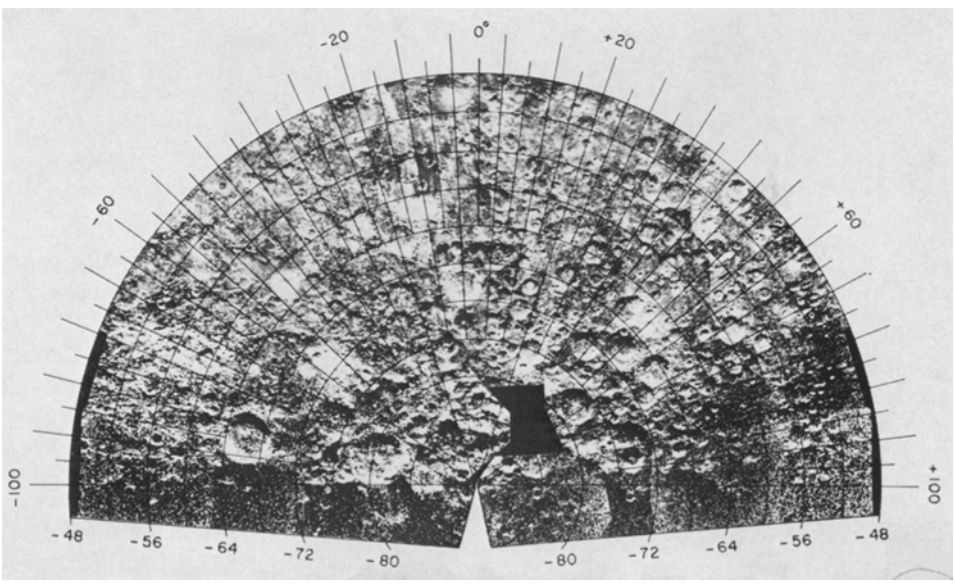

(b)

Fig. 8. South Polar Belt: (a) Polarized, (b) Depolarized.

whereas the polarized maps emphasize the quasi-specular component, because of its much greater strength relative to the diffuse component in these maps. The appearance of pseudo-highlights and shadows on the polarized maps and on the limb areas of the depolarized maps, of course, is a consequence of the slope of the mean lunar scattering law (Figure 10).

Because of the high resolution of the measurements, publication of the entire data set on a sufficiently small scale to show all the wealth of detail would be unacceptably bulky. We can provide, for limited areas, the detailed maps, printed quantitative data, or tape copies from the Haystack Data Library. For these reasons, therefore, the enlarged maps in Figures 4–7 are mosaics of 10 to 15 ZAC-maps each, covering an area of about 10^6 km^2. A few individual ZAC areas are presented below.

As an illustration of the large amount of information available in the radar maps, Figure 9a shows a area small in Oceanus Procellarum, just west of the crater Kepler.

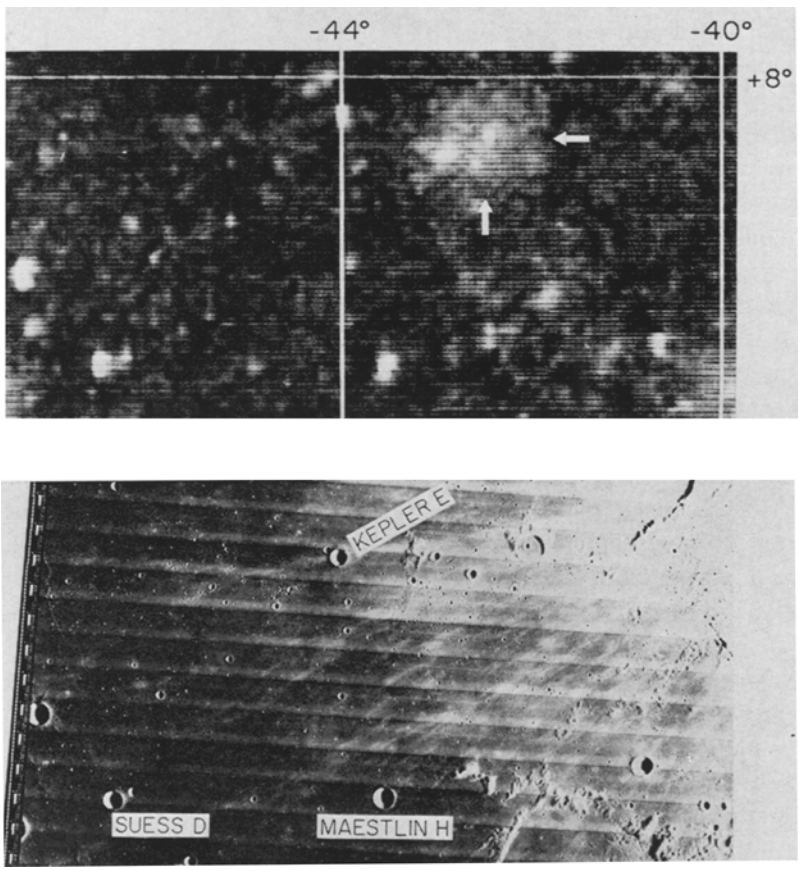

Fig. 9. Expanded-scale maps of the lunar surface west of the crater Kepler, showing the correlation between radar features and small craters. (a) 3. 8 cm radar map from ZAC 5.23, (b) Lunar Orbiter photograph from Mission IV, Frame H-144, same scale and coverage as (a).

For comparison, Figure 9b is a portion of a Lunar Orbiter photograph of the same area, on the same scale. At least three categories of radar features can be distinguished within this area: (1) well-defined, named craters; (2) very small, un-named craters; and (3) a radar anomaly with no apparent optical counterpart.

The radar map clearly shows a number of large, relatively bright spots that are coincident with moderate-size (5 to 10 km) craters including Suess D, Maestlin H and Kepler E. In addition, however, there are numerous small radar spots that turn out in most cases to coincide with very small, young-appearing craters on the Orbiter picture. One noteworthy observation is that the strength or size of the radar features in this class is not necessarily correlated with the apparent size or optical albedo of the crater.

As an extreme example, note the feature located about 20 km northwest of Suess D and south of the unlabeled 5-km crater Reiner B. Here, the radar echo is about as bright and as large as that of Kepler E, although the optical photographs shows only a few small craters no different in individual appearance or in number than most of the nearby area within a radius of 100 km. Several other examples of such bright spots can be seen north and northeast of Reiner B.

The anomalously strong radar return from these small craters could have a number of causes. Originally it was thought that only a rocky ejectra blanket could give rise to a strong depolarized return. After some experience with the Apollo landing sites (Zisk and Moore, 1972) it appears that a high density of surface rocks is not at all well correlated with the strength of the diffuse radar echoes, and that perhaps, as Pollack and Whitehill (1972) have suggested, the small-scale topography of craters is responsible for the largest part of even the depolarized radar echoes. The correlation between halo brightness and radar echo strength, then, can be attributed to meteoric erosion. Craters that are young enough to retain a bright halo also have the sharp contours and steep inner slopes of their recent origin, whereas older craters whose original halo is no longer visible also possess a shallow, subdued topography. The latter would hence have no rough inner surfaces tilted steeply toward the Earth-based radar and would not be as able to depolarize the radar echoes by the hypothesized double scattering.

There is additional evidence that multiple scattering causes at least a part of the depolarized (diffuse) component of the polarized backscatter. Figure 10 shows the average normalized radar backscattered power derived from all the measurements in the program, plotted as a function of angle of incidence. Only uncalibrated measurements were excluded (less than 10% of the whole). To produce the graphs of Figure 10 each ZAC-map was divided into 25 equal sub-areas; the true angle of incidence, θ, at the center of each sub-area was calculated for the time of the observation, and the echo strengths of all measured points in the sub-area were averaged after the originally-assumed scattering law (see Table I) was removed.

The resulting graphs follow very closely the earlier scattering-law measurements reported by Evans (Evans and Hagfors, 1971) for the polarized echo, and a $(\cos\theta)$ dependence for the depolarized echo. Wide deviations at the lower angles of incidence are undoubtedly the result of the intentional scarcity of measurements near the sub-radar point, a deliberate result of our desire for well-resolved surface maps (see Article I).

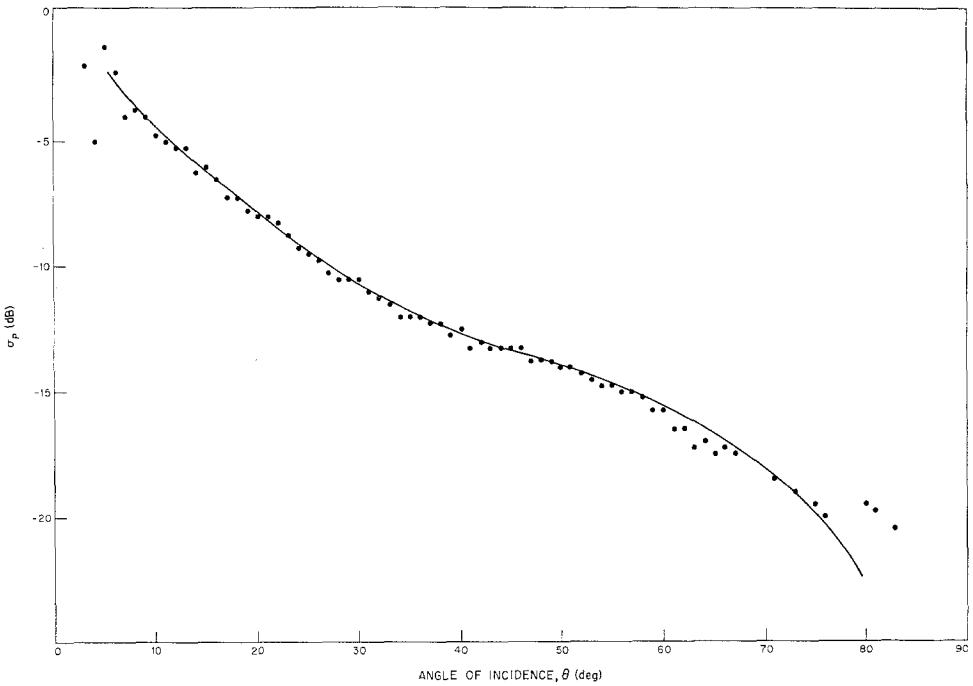

Fig. 10. Observed mean backscattered power vs angle of incidence at 3.8 cm: (a) Polarized signal, (b) Depolarized signal.

An interesting feature of these curves is the narrow dip in the backscattered power at 63° angle of incidence, in both the polarized and depolarized echoes. One explanation for this effect, and possibly the most reasonable of a number of generally unsatisfactory explanations, is that both the depolarized and the diffuse-polarized echoes are

generated by double reflections, with the uppermost horizontal layer of soil acting in most cases as one of the reflecting surfaces. In this event, one linearly-polarized component of the incident radiation would be transmitted most strongly into the surface layer at the Brewster angle and would then not be available to contribute to the backscattered signal.

If the dip at 63° is connected with the Brewster angle, it implies an average dielectric constant of 3.9 for the surface layer, which is somewhat higher than deduced from other radar measurements (Tyler, 1968).

Further analyses of the scattered signal-strengths and originating reflections mechanisms would not be justified at this time, since the accuracy required of the data is much greater than that which is at present available. A search of the data for systematic effects or for chance effects of lunar surface characteristics is, however, reasonable and is to be carried out.

Although radar backscatter may well be controlled by topography, some surface features are, nevertheless, most probably the result of a widespread distribution of radar scatterers such as rocks. One striking example of such a feature is the bright, diffuse area indicated by the white arrows on the radar map of Figure 9a. There is no obvious indication on Figure 9b, the optical photograph, of any reason for this 50 km diam area of high radar backscatter. It is seen from the optical photograph to be located within the bright ray pattern of the crater Kepler. As expected, however, no other indication of Kepler's ray pattern is visible on the radar map. Most lunar rays are known, both from earth-based observations at low sun-angle and from Apollo surface observations, to be thin deposits of generally fine-grain material, and as such would not produce an enhancement in radar backscatter. It is possible, however, that the bright radar spot was created by a coherent clod of material thrown out of Kepler along with the ray material, presumably at the time the crater was formed. There is another more certain example of such a coherent ejectum from the crater Tycho: The radar-bright crater complex surrounding Hell QW (3.5° W, 32.5° S on Figure 7.3b). This feature is located on one of the three Tycho rays that are dense enough to appear on the radar map. An optical photograph of the area shows not only a profusion of craters, but also crater strings and elongations that are aligned with a radius from Tycho (at 10° W, 43° S: Figure 7.3b). The circular shape of both the Hell QA and Kepler radar enhancements also argue in favor of an origin by the low-velocity impact and disruption of a loosely-cohesive body.

In summary, this small area in Figure 9 contains examples of the most common general causes of well-defined 3.8 cm radar enhancements: The moderate size craters which are radar backscatterers for various reasons; the very small, young craters, which may exhibit large radar-backscatter enhancements in surface area and in strengths, either from their blocky ejecta blankets or their extreme inner topography; and the diffuse, optically unremarkable enhanced areas probably originating in a field of rocks or of jagged topography often of uncertain origin. In Article IV we shall treat the spectrum of radar enhancements in more detail, bringing in additional information to help judge the lunar surface conditions that might give rise to the observations.

In addition to the characterization of small-scale features, the lunar radar data should also contain evidence about surface conditions on a larger scale. Several papers have already been prepared that attempt this type of analysis (Zisk *et al.*, 1971; Pieters *et al.*, in press; Zisk and Moore, 1972; and Moore and Zisk, to be published). In Appendix A, we present another series of brief descriptions of a number of lunar regions once considered as candidates for Apollo landings, some of which were, in fact, made within the described regions. It should be noted that these descriptions date from before the Apollo 14 and subsequent landings, and are presented here in that unsophisticated state to demonstrate the information that can be extracted from earth-based radar alone.

Acknowledgments

The 3.8-cm mapping of the lunar surface in two polarization received vital cooperation and enthusiasm from many members of the Haystack Research Facility and Lincoln Laboratory, including H. H. Danforth, J. V. Evans, R. P. Ingalls, M. H. Leavy, J. I. Levine, L. P. Rainville, A. E. E. Rogers, P. B. Sebring and many others. Special thanks are due to T. Hagfors for making so freely available his time and his extensive knowledge of lunar scattering processes. Modification and new construction of equipment was ably accomplished by W. J. O'Donnell, R. J. Cady, J. M. Sobolewski, and others. The development of the voluminous computer programs to plan and carry out the measurements and process and display the backscatter data was carried out in large part by R. A. Brockelman, G. W. Armistead, and A. D. Kaminsky.

The work was supported by NASA Manned Spacecraft Center Contract NAS 9-7830. We gratefully acknowledge the cooperation of the U.S. Air Force in making available the Haystack Research Facility.

Appendix A

RADAR CHARACTERISTICS OF PROPOSED APOLLO LANDING SITES

We have examined the radar data for most of those sites that have been considered for Apollo landings beyond Apollo 12, with the exception of several of the original mare sites. Our conclusions are presented below. There appears to be a reasonable correlation between our results and those from other sources, although the descriptions given here are mainly qualitative in nature.

Hyginus Rille: (6.4° E, 8.0° N)
Although the general area is covered by strong radar anomalies (notably the string of craters scattered along the rille), the proposed landing site is on a small area of low radar backscatter and hence apparently has a relatively smooth and rock-free surface. The area of radar darkness coincides with the smooth, dark area on optical photographs and may be either a recent flow or an overlying layer of soil, relatively thick (a meter or more) or compact, since there is no sign on the radar maps of the rocks which presumably have been covered. Examination of the large circular crater at the

bend in the rille indicates no unusual rockiness on its floor, but there is quite a strong indication of rockiness in the elongated crater that protrudes northward toward the proposed landing site. This enhancement appears confined to the crater itself and ends with a sharply defined transition to the dark area containing the landing site. There appear to be a number of markedly different geological units available for sampling in a relatively small area.

Descartes: (15.6° E, 8.9° S – Near the Actual Apollo 16 Landing Site)
The radar measurements of this site were puzzling, in that the polarized backscatter for the area is well below average, whereas the depolarized is equal to or slightly higher than average. One strong possibility, borne out during the landing, was that the rockiness of the site is about the same as for Apollo 11 and 12 (giving rise to an average depolarized return), but that the soil is much less reflective – perhaps because of a higher porosity – over the entire floor of the large, eroded crater on whose eastern edge the landing site is located.

The two bright, small craters 10 km to the south and 4 km to the northeast (later named South Ray and North Ray crater) show up clearly as strong radar anomalies and were expected to provide an interesting geochemically contrasting surface sample if a traverse were to be extended toward either one.

Davy Rille: (6.0° W, 10.9° S)
This site is located in an area of extremely low radar backscatter. Both polarized and depolarized values are 0.3 times the average for this angle of incidence, which suggests that only a very small percentage of the surface could be rocky, and also that the soil may be unusually porous and consist mainly of low-dielectric-constant minerals. The enhancement along the crater chain of the rille is well marked against such a background, but even these craters exhibit low backscatter values, typically 0.6 times average. It is possible that the craters merely expose the more highly compacted soil some meters below the surface; from the radar results, it appears likely that there is not much rock within the craters either.

Fra Mauro: (17.6° W, 3.6° S)
This is another area that was actually the site of a landing (Apollo 14). It is a comparatively featureless area. The polarized backscatter over the 20-km neighbourhood is less than half the average for the angle of incidence, indicating a smooth surface, presumably with a thick regolith layer and sparse or heavily eroded surface rocks. There are few indications of recent cratering and even those are relatively subdued. These indications are similar to the Apollo 11 and 12 landing areas, but more extremely subdued. The dustiness observed at the landing site corroborated these preliminary interpretation.

Hadley-Apennines: (2.5° E, 24.8° N – Well south of Apollo 15 landing site, on similar terrain)
This is a complex area on the radar maps. For a complete treatment of the general

region and the Apollo 15 landing site in particular, see Zisk *et al.* (1971). The low (0.15 times average) depolarized return at the proposed landing site itself indicates few rocks, although the optical photos show a substantial amount of cratering. This suggests a thick, eroded regolith layer.

There is a considerable increase in rockiness indicated on the depolarized radar map about 6 to 8 km to the south, and a strong return from the rille itself and from the hills to the east and west.

The polarized return (about 0.9 times average) substantiates the reduced rockiness at the site, but is not so clear about the rille and the surrounding hills, probably because of the rolling nature of the terrain and the resulting variations caused by local surface tilts.

Copernicus Peaks: (19.9° W, 9.9° N)

From the radar maps, the proposed landing site appears to be well chosen for the floor of Copernicus, with backscatter values that are near to the lowest in a 20-km circle. These values are nevertheless 1.5 and 3 times the general averages at this angle of incidence for polarized and depolarized radar, respectively, which fact confirms the expectation that the floor of Copernicus will be a very rough area, with a relatively large fraction of the surface covered by exposed and nearly exposed rock. The sizes of these rocks, however, need not be very great to produce the observed radar picture. (The modal values for polarized and depolarized return, within a circle of 20-km radius centered on the proposed landing site, are about 2.3 and 4 times the corresponding general averages, compared with 1.5 and 3 for the landing site.)

Littrow: (28.9° E, 21.7° N – Some distance from the Apollo 17 site, on a different geologic unit)

This area is located on a region with one of the lowest values of depolarized backscatter of the entire 3.8-cm radar map, about 15% of the average for its angle of incidence. The Littrow surface should therefore yield a very low fraction of rocks for astronaut sampling. It would be very interesting to discover whether the geochemistry and/or age of the surface material could yield any clue as to the origin of this finely divided or unbroken surface layer, or whether the on-site exploration reveals another unexpected reason for the anomalously weak radar return.

Censorinus: (32.6° E, 0.4° S)

The entire area surrounding the crater exhibits unusually strong enhancement. At the location of the proposed Apollo landing site, the backscatter has dropped well below the extreme value around the crater itself, and is somewhat lower than the average for its angle of incidence. (At the crater both the polarized and depolarized backscatters are about twice the average.) One would expect the surface to be rocky to about the same extent as Apollo 11 and 12 landing sites, or perhaps slightly more. It would be very interesting to obtain a size-distribution count and some sort of 'jaggedness factor' for the proposed landing area for the traverses extending toward the crater. This would

provide information on the effect of jagged vs smooth rocks on the radar return and might contribute to an improved theory of radar scattering by the lunar surface which could then be applied to the radar data from additional unexplored areas.

Tycho Rim: (11.3° W, 40.9° S)
At Tycho, the angle of incidence is large (> 50°) and interpretation of the radar maps must be carried out with more caution. As pointed out earlier, the effect of local tilts on the backscattered power at such large angles of incidence has become significant in the depolarized map, and must be separated out from the physical character of the surface itself which is of primary concern here.

From both optical and radar pictures, the area surrounding the proposed landing site is relatively flat, and the radar should give a fairly good idea of the surface structure. The polarized and depolarized values are about 1.4 and/1.8 times the average for this angle of incidence, indicating as expected, that the area is considerably rockier than average. As in the case of the proposed Copernicus landing site, the radar shows that the 2 km × 2 km Tycho site is by far the smoothest for 20 km around. The modal backscatter values elsewhere in the neighborhood are about 2.0 and 2.5 times the corresponding averages.

Marius Hills: (56.6° W, 14.6° N)
There is no bold relief apparent in this area which might have complicated the interpretation of the radar maps at this high angle of incidence. A number of features show up on both polarized and depolarized radar maps, but none are very strong and the general values of backscatter are about average (1.0 to 1.3 times the average for this angle of incidence). The hills do not appear unusually enhanced, and so should be well covered with soil. There are no indications of large-scale rocky protuberances. From the radar measurements the surface somewhat similar to the Apollo 11 and 12 sites, although one must keep in mind that the radar results are not greatly influenced by the chemistry or age of the surface, except indirectly by the state of erosion of surface rocks.

References

Evans, J. V. and Hagfors, T.: 1971, in *Adv. Astron. and Astrophys.*, Academic Press, New York and London, pp. 29–105.
Moore, H. J. and Zisk, S. H.: 1973, 'Calibration of Radar Data from Apollo 17 and Other Mission Results', submitted for *Apollo 17 Preliminary Science Report*, NASA; to be published.
Pettengill, G. H. and Thompson, T. W.: 1968, *Icarus* **8**, 457–471.
Pettengill, G. H., Zisk, S. H., Thompson, T. W.: 1973, *The Moon*, this issue, p. 3.
Pieters, C., McCord, T. B., Zisk, S. H., and Adams, J. B.: 'Lunar Black Spots and the Nature of the Apollo 17 Landing Area', *J. Geophys. Res.*, to be published.
Pollack, J. B. and Whitehill, L.: 1972, *J. Geophys. Res.* **77**, 4289–4303.
Thompson, T. W.: 1973, *The Moon*, this issue, p. 51.
Tyler, G. L.: 1968, *Nature* **219**, 1243–1244.
Zisk, S. H. and Moore, H. J.: 1972, *Apollo 16 Preliminary Science Report*, NASA SP-315, Government Printing Office.
Zisk, S. H., Carr, M. H., Masursky, H., Shorthill, R. W., and Thompson, T. W.: 1971, *Science* **173**, 808–811.